nature chemistry

Article

https://doi.org/10.1038/s41557-022-01061-5

Quantum nanomagnets in on-surface metal-free porphyrin chains

Received: 1 June 2021

Accepted: 9 September 2022

Published online: 24 October 2022

Check for updates

Yan Zhao[1,7], Kaiyue Jiang[2,7], Can Li[1,7], Yufeng Liu[1], Gucheng Zhu[1], Michele Pizzochero[3], Efthimios Kaxiras[3,4], Dandan Guan[1,5,6], Yaoyi Li[1,5,6], Hao Zheng[1,5,6], Canhua Liu[1,5,6], Jinfeng Jia[1,5,6], Mingpu Qin[1,5], Xiaodong Zhuang[2] ✉ and Shiyong Wang[1,5,6] ✉

Unlike classic spins, quantum magnets are spin systems that interact via the exchange interaction and exhibit collective quantum behaviours, such as fractional excitations. Molecular magnetism often stems from *d*/*f*-transition metals, but their spin–orbit coupling and crystal field induce a significant magnetic anisotropy, breaking the rotation symmetry of quantum spins. Thus, it is of great importance to build quantum nanomagnets in metal-free systems. Here we have synthesized individual quantum nanomagnets based on metal-free multi-porphyrin systems. Covalent chains of two to five porphyrins were first prepared on Au(111) under ultrahigh vacuum, and hydrogen atoms were then removed from selected carbons using the tip of a scanning tunnelling microscope. The conversion of specific porphyrin units to their radical or biradical state enabled the tuning of intra- and inter-porphyrin magnetic coupling. Characterization of the collective magnetic properties of the resulting chains showed that the constructed $S = 1/2$ antiferromagnets display a gapped excitation, whereas the $S = 1$ antiferromagnets exhibit distinct end states between even- and odd-numbered spin chains, consistent with Heisenberg model calculations.

Molecular nanomagnets have been proposed as promising candidates for information storage, molecular spintronics and quantum computing. Porphyrins and related macrocycles have excellent stability, high chemical versatility, as well as the ability to stabilize different ions at their centre, which potentially allows for the tuning of their biological, electronic and magnetic properties[1–4]. Although individual magnetic porphyrins have been widely studied and are well understood, little is known about the coupled spins in multi-porphyrin systems. The magnetism of a porphyrin macrocycle typically comes from its central magnetic metal ion, in which any unpaired *d*/*f* electrons highly localize at the centre. This localization means that the spins in assembled porphyrin architectures undergo a negligible magnetic exchange interaction. In the past decade, a series of porphyrin architectures have been achieved on surfaces, including single porphyrin molecules, covalent porphyrin polymers and self-assembled nanostructures[1,3,5–17]. However, none has exhibited detectable collective magnetic behaviours, where the spins are correlated together and undergo collective excitation.

Recently, delocalized π-electron magnetism has been introduced in porphyrins through engineering of their π-electron topologies[18–20]. This delocalization effect allows for further realization of quantum nanomagnets with coupled spins in covalent porphyrin architectures. However, due to their high reactivity and/or low solubility,

[1]Key Laboratory of Artificial Structures and Quantum Control (Ministry of Education), Shenyang National Laboratory for Materials Science, School of Physics and Astronomy, Shanghai Jiao Tong University, Shanghai, China. [2]The meso-Entropy Matter Lab, School of Chemistry and Chemical Engineering, Shanghai Jiao Tong University, Shanghai, China. [3]School of Engineering and Applied Sciences, Harvard University, Cambridge, MA, USA. [4]Department of Physics, Harvard University, Cambridge, MA, USA. [5]Tsung-Dao Lee Institute, Shanghai Jiao Tong University, Shanghai, China. [6]Shanghai Research Center for Quantum Sciences, Shanghai, China. [7]These authors contributed equally: Yan Zhao, Kaiyue Jiang, Can Li. ✉e-mail: zhuang@sjtu.edu.cn; shiyong.wang@sjtu.edu.cn

https://doi.org/10.1038/s41557-022-01061-5

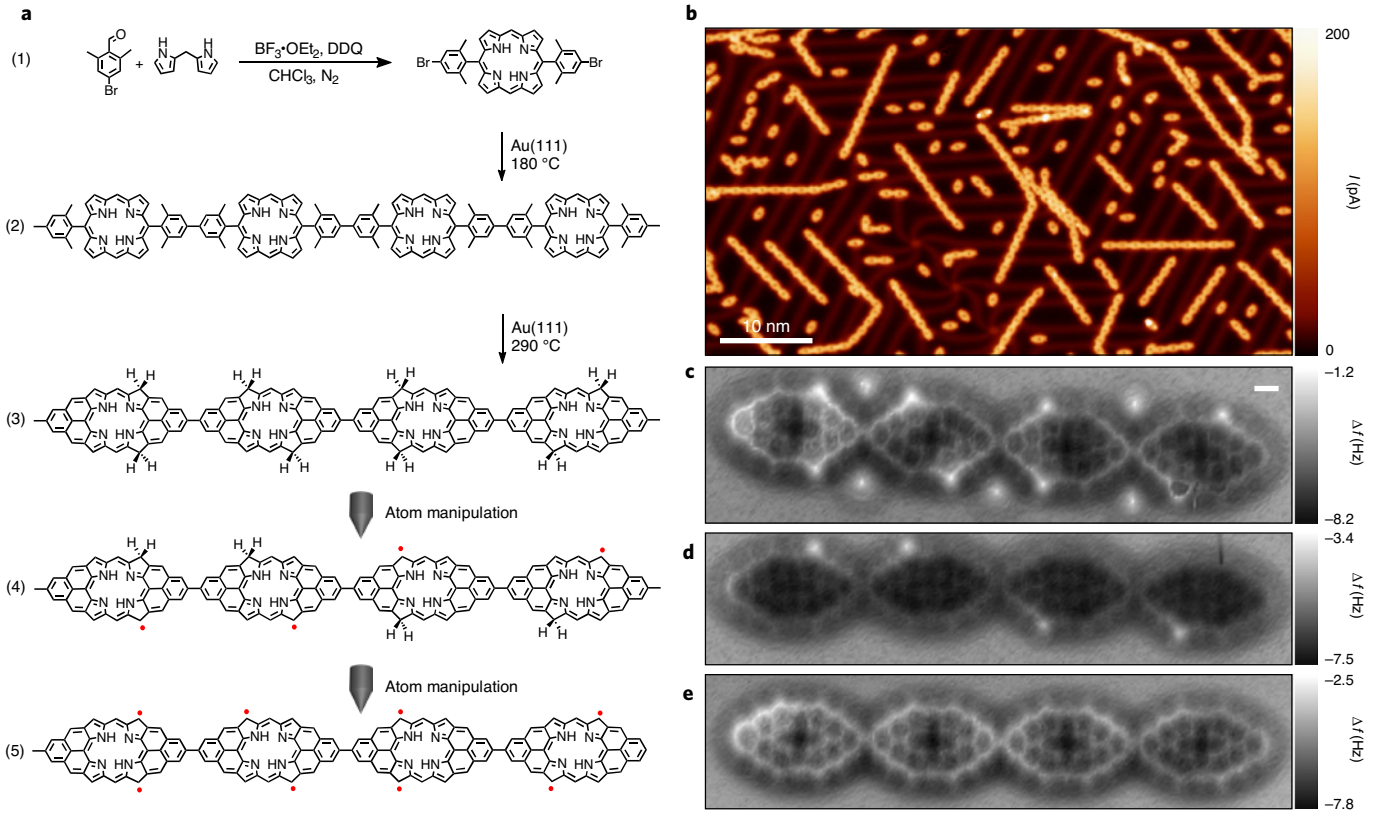

Fig. 1 | Construction of molecular nanomagnets in metal-free porphyrins. **a**, Synthetic route for the construction of molecular nanomagnets through three sequential steps: (1) in-solution synthesis, (2, 3) on-surface synthesis and (4, 5) atom manipulation. Red dots represent the unpaired π electrons. **b**, Large-scale constant-current STM image (bias, 1 V; current, 20 pA). The on-surface synthesis approach yields porphyrin chains with different lengths. **c**–**e**, nc-AFM frequency-shift images of a closed-shell porphyrin chain (**c**), $S = 1/2$ porphyrin chain (**d**) and $S = 1$ porphyrin chain (**e**) (resonant frequency, 28 kHz; oscillation amplitude, 100 pm; scale bar, 0.3 nm) with the bright protrusions at the edges indicating sp^3 carbon sites. Through atom manipulation, the sp^3 carbon can be transformed into an sp^2 carbon by dissociating one hydrogen. Using the three-step method depicted in **a**, molecular quantum nanomagnets can be built, spin by spin.

it has remained challenging to synthesize such porphyrin quantum nanomagnets by traditional 'wet' chemistry. Pioneered by Grill and colleagues in 2007, on-surface synthesis has become a powerful approach for the fabrication of atomically precise covalent nanostructures, with milestones including single molecules, covalent porphyrin polymers, graphene nanoribbons and two-dimensional (2D) covalent molecular frameworks[21–31]. Meanwhile, the atom manipulation approach has been developed by Hla, Gross and colleagues for studying individual chemical reactions in real space by using an atomically sharp metal tip, with outstanding examples being the syntheses of biphenyl molecules, triangulene nanographenes, *sp*-hybridized carbon chains and rings, to name a few[32–36]. These two approaches are complementary to each other, as on-surface synthesis enables the synthesis of large repeated nanostructures, and atom manipulation is effective for building single, complex custom-designed structures.

In this Article we take advantage of both on-surface synthesis and the atom manipulation approach to construct complex, custom-designed molecular nanomagnets in metal-free porphyrins, spin by spin on a Au(111) surface. On-surface synthesis is used to construct extended porphyrin chains with two sp^3 carbon sites per porphyrin unit, forming an extended 1D sp^3 carbon lattice. Through atom manipulation, one of the two hydrogens in each sp^3 carbon site can be controllably dissociated at predefined locations in the sp^3 carbon lattice. Each hydrogen-dissociation step transforms an sp^3 carbon into an sp^2 carbon, and thus introduces one delocalized π radical into the aromatic system. The delocalized character of π-electron magnetism gives rise to a considerable intra-unit as well as inter-unit magnetic coupling, allowing for the construction of quantum nanomagnets with tunable magnetic exchange interactions. A series of molecular nanomagnets were constructed and thoroughly characterized by non-contact atomic force microscopy (nc-AFM) and scanning tunnelling microscopy/spectroscopy (STM/STS) together with density functional theory (DFT) calculations and theoretical modelling. Our results show that the two spins inside each porphyrin unit are ferromagnetically coupled with an intra-unit magnetic exchange strength of 20 meV, and the spins between two neighbouring porphyrin units are antiferromagnetically coupled with an inter-unit magnetic exchange strength of ~3 meV. Additionally, different quantum phases have been observed in the constructed molecular nanomagnets, such as gapped excitations in finite $S = 1/2$ antiferromagnetic nanomagnets, and zero-mode end states in $S = 1$ antiferromagnetic nanomagnets. The ability to construct coupled spins one by one provides ample opportunities for exploring the new exotic phases of quantum magnetism in organic nanomagnets.

Results and discussion

Synthesis and structural characterization

Figure 1a presents the three-step scheme—precursor synthesis, on-surface synthesis and atom manipulation—to construct quantum nanomagnets, spin by spin, in porphyrin chains. The precursor 5,15-bis(4-bromo-2,6-dimethylphenyl)porphyrin is synthesized in solution by traditional 'wet' chemistry (Supplementary Fig. 1). After in-solution synthesis, the precursor is thermally deposited on Au(111) held at 180 °C, followed by a subsequent annealing to 290 °C for 10 min. With thermal activation, carbon–carbon coupling and cyclodehydrogenation reactions take place, giving rise to fully aromatic

https://doi.org/10.1038/s41557-022-01061-5

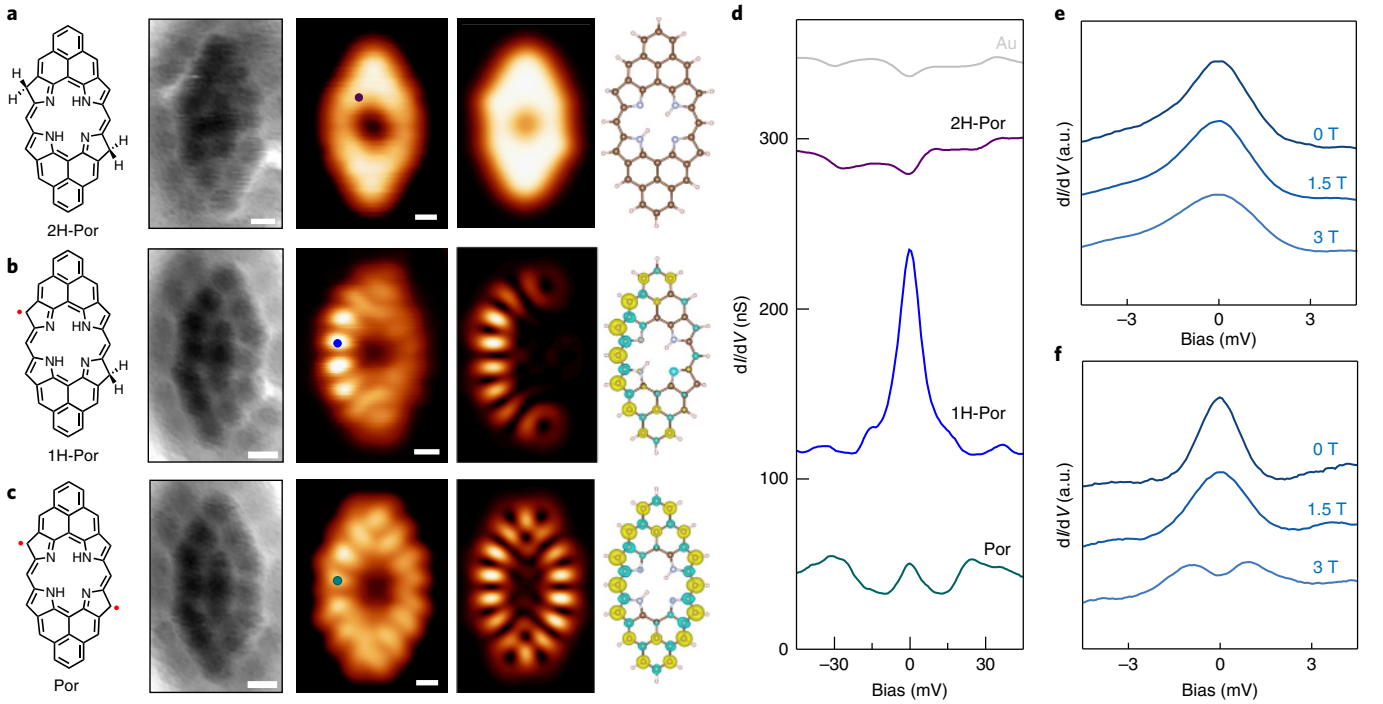

Fig. 2 | Characterization of intra-unit magnetic coupling within porphyrin monomers. a–**c**, Characterization of 2H-Por (**a**), 1H-Por (**b**) and Por (**c**). From left to right: chemical structure, nc-AFM image (resonant frequency, 28 kHz; oscillation amplitude, 100 pm; scale bars, 0.2 nm), constant-height current image (bias voltage, 10 mV; scale bars, 0.2 nm), simulated constant-height STM image and spin density distributions (green, spin up; yellow, spin down). For the simulated structures (right panels), the bottom hydrogen on each sp^3 carbon is hidden in this top view, although one can see that the visible C–H bond is slightly shorter than those of the of sp^2 carbons. The generated unpaired spin delocalizes at one side of the molecule. **d**, d*I*/d*V* spectra taken on the locations marked in the constant-height current images in **a**–**c**. The presence of net spin and the intra-molecular magnetic exchange interaction are confirmed by showing Kondo resonance and spin-flip features. **e**,**f**, The Kondo resonance peaks of $S = 1/2$ (**e**) and $S = 1$ (**f**) as a function of applied vertical magnetic field. The spectra are shifted vertically for clarity. The Kondo resonance of the high spin $S = 1$ is more sensitive to the magnetic field, suggesting its underscreened nature.

porphyrin chains of different length (Fig. 1b; the length distribution is shown in Supplementary Fig. 5). Bond-resolved nc-AFM imaging was used to characterize the chemical structure of the achieved products by functionalizing a CO molecule at the tip apex[37]. The nc-AFM image in Fig. 1c shows that each porphyrin unit is composed of two sp^3 carbon sites, which appear as shallow protrusions located randomly at two outer corners of the porphyrin macrocycle. We attribute the high yield of sp^3 carbon sites to the diradical character of each porphyrin unit (see the Clar non-Kekulé structures in Supplementary Fig. 3). During the cyclodehydrogenation reaction process, the dissociated hydrogen atoms migrate on the surface and saturate the radical sites, forming two sp^3 carbon sites per porphyrin unit. For comparison, we studied the 5-(2,6-dimethylphenyl)porphyrin precursor, which results in products with a closed-shell electronic structure after cyclodehydrogenation. As expected, none of the products feature any sp^3 carbon sites (details are provided in Supplementary Fig. 4). Through atom manipulation, we can controllably dissociate one hydrogen from an sp^3 carbon site by injecting inelastic tunnelling electrons (see the *I*–*V* curve in Supplementary Fig. 2), which transforms an sp^3 carbon into an sp^2 carbon (radical), thus introducing an unpaired π electron into the aromatic system. Using the above strategy, we constructed two typical examples of porphyrin nanomagnets holding four and eight unpaired spins, as confirmed by high-resolution nc-AFM imaging (Fig. 1d,e); these can be simplified as a finite $S = 1/2$ and $S = 1$ antiferromagnetic spin chain, respectively (vide infra). Note that all the porphyrin chains are adsorbed flat on the Au(111) due to their tight physisorption, although a twisted configuration is expected in the gas phase (see the DFT-optimized structure in Supplementary Fig. 15).

Intra-unit magnetic exchange interaction

Intra-unit magnetic coupling between the two spins within a porphyrin monomer was studied by means of STS measurements, together with DFT calculations and theoretical modelling. As shown in Fig. 2, we dissociated one hydrogen away from each of the two sp^3 carbon sites, one by one, and traced their magnetic ground states. We refer to the porphyrin monomer with two, one and zero sp^3 carbon site(s) as 2H-Por, 1H-Por and Por, respectively. Both spectroscopic measurements and DFT calculations confirm that the 2H-Por has a closed-shell electronic structure (Fig. 2a,d). The 2H-Por converts into 1H-Por after the bias voltage is slowly ramped to 3 V by positioning the STM tip above the sp^3 carbon site and retracting 400 pm away from a tunnelling setpoint of $V = 10$ mV and $I = 10$ pA. The 1H-Por features an odd number of π electrons, with a magnetic ground state of $S = 1/2$ as shown by DFT calculations (Fig. 2b). Using the same procedure, the 1H-Por is further manipulated into Por, as shown in Fig. 2c; this has two unpaired π electrons. DFT calculations suggest that the two spins reside at opposite sides along the long axis of the monomer, with a ferromagnetic coupling of 15 meV. The presence of delocalized magnetism in π-conjugated systems is due to the minimization of on-site Coulomb repulsion, which can be qualitatively captured by mean-field DFT calculations, but higher levels of calculations including correlation effects are required to quantitatively address these systems[38]. In the following we have mainly performed DFT calculations in the gas phase to analyse our measurements. Spin-flip spectroscopy measurements confirm the magnetic exchange interaction by showing two symmetric steps above/below the Fermi level at 20 mV (Fig. 2d); this is due to the presence of a spin-flip tunnelling channel induced by inelastic tunnelling electrons[39,40]. Additionally, the presence of net spins in 1H-Por and Por

https://doi.org/10.1038/s41557-022-01061-5

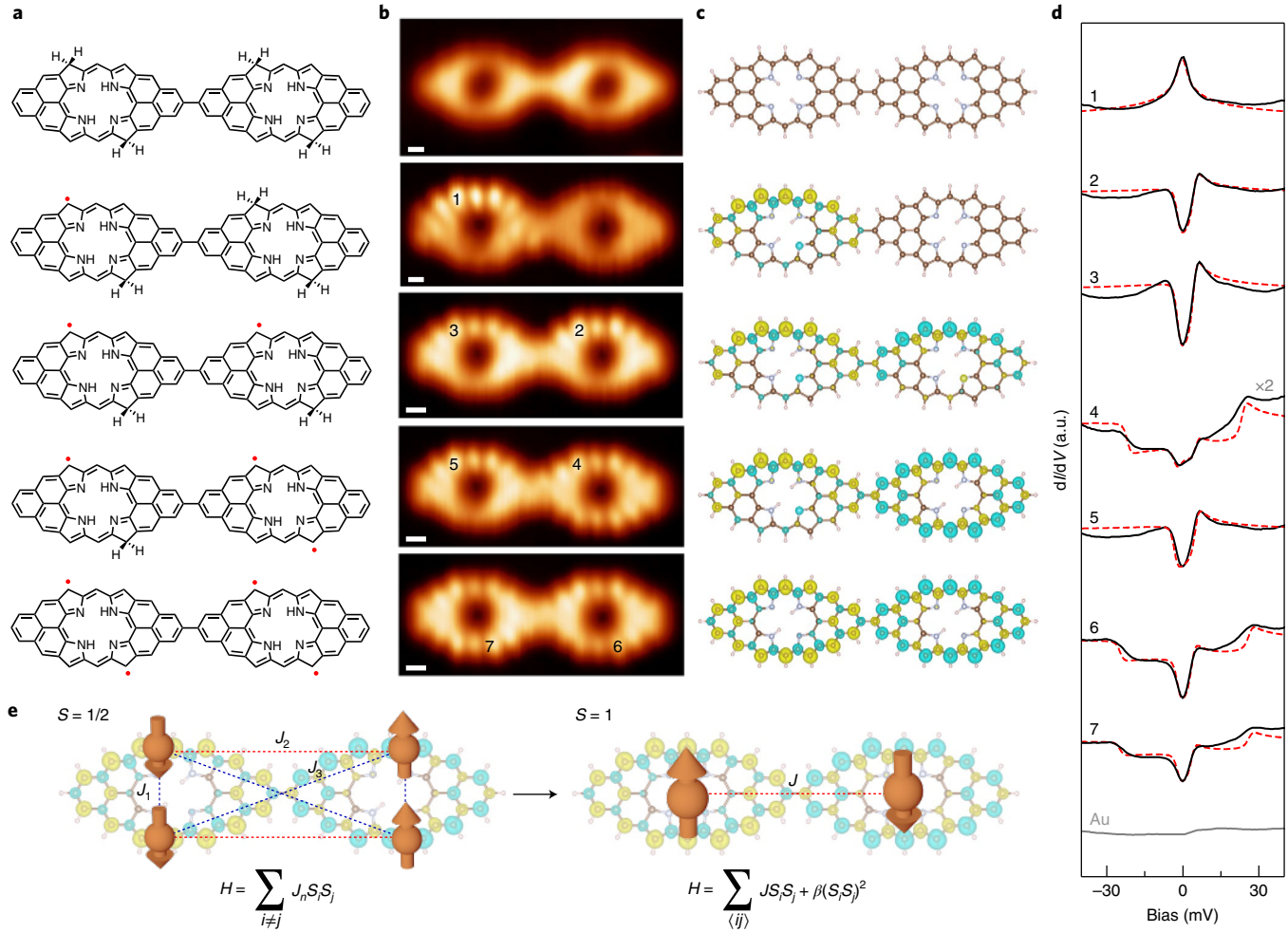

Fig. 3 | Characterization of inter-unit magnetic coupling within porphyrin dimers. a–**c**, Five different porphyrin dimers, prepared on a Au(111) surface, that feature different numbers of unpaired spins: chemical structure (**a**), constant-height current image (**b**) (bias voltage, 10 mV; scale bars, 0.2 nm) and simulated structures and spin density distributions (**c**) (green, spin up; yellow, spin down) of porphyrin dimers. For the simulated structures (**c**), the bottom hydrogen on each sp^3 carbon is hidden in this top view, although one can notice that the visible C–H bond is slightly shorter than those of sp^2 carbons. **d**, d*I*/d*V* spectra taken on the locations as marked in the constant-height current images in **b** (black solid lines) and simulated local density of states (LDOS) spectra obtained by using a perturbative approach (red dashed lines). The step features indicate intra- and inter-unit magnetic exchange coupling. The intensity of spectrum 4 has been doubled for comparison purposes. **e**, Left: schematic of the intra- and inter-unit magnetic coupling among the four $S = 1/2$ spins in the dimer, with parameters of $J_1 = -20$ meV, $J_2 = 3.2$ meV and $J_3 = 2.4$ meV to fit the experimental spectra in **d**. Right: simplified antiferromagnetic coupled $S = 1$ model, with $J = 2.8$ meV and $\beta = 0.001J$, obtained by $S = 1$ bilinear–biquadratic model fittings.

was further confirmed by the Kondo resonance effect. The Au(111) surface electrons screen the net spin(s) and result in a many-body Kondo resonance, showing a sharp peak at the Fermi level. As shown in Fig. 3d, Kondo resonances have been observed in both 1H-Por and Por. However, the Kondo resonance intensity of spin $S = 1/2$ in 1H-Por is significantly stronger than that of spin $S = 1$ in Por. This difference is due to the different screening effects; the quantized spin $S = 1/2$ is completely screened by Au(111) conduction electrons, whereas the higher spin $S = 1$ is underscreened (partially screened with a remaining magnetic moment), in agreement with theory predictions and recent experimental observations on magnetic nanographenes[41,42]. This difference in Kondo screening was further confirmed by d*I*/d*V* spectra under an out-of-plane magnetic field. As shown in Fig. 2e,f, the Kondo resonance of $S = 1/2$ is robust against the magnetic field, but the Kondo resonance of $S = 1$ is extremely sensitive to the applied magnetic field due to its underscreened nature, with Zeemann splitting energy much smaller than the Kondo temperature[43] (the Kondo temperature estimation is shown in Supplementary Fig. 7). We simulated the observed d*I*/d*V* spectra by using a perturbative approach as established by Ternes[39], which nicely reproduced the experimental features (Supplementary Fig. 17).

Inter-unit magnetic exchange interaction

Inter-unit magnetic coupling was studied by constructing four spins, one by one, in a covalent porphyrin dimer (Fig. 3). A π radical was first created inside the dimer; this localizes at the dehydrogenated side, exhibiting a sharp Kondo resonance in the d*I*/d*V* spectrum (Fig. 3d). In the second step, we deliberately created another π radical inside the other unit of the dimer to show the inter-unit magnetic coupling. DFT calculations suggest that the two spins are antiferromagnetically coupled with an inter-unit exchange strength of 2.1 meV if the two spins are resident on the same side along the long axis of the dimer, and 1.8 meV when the two spins are on opposite sides (Supplementary Fig. 9). The d*I*/d*V* spectra in Fig. 3d confirm this antiferromagnetic coupling by showing a spin-flip feature below and above the Fermi level at 3.2 mV. For comparison, a porphyrin dimer with two radicals located at opposite sites was constructed; this exhibits a spin-flip feature at 2.4 mV, qualitatively agreeing with the DFT calculations (Supplementary

https://doi.org/10.1038/s41557-022-01061-5

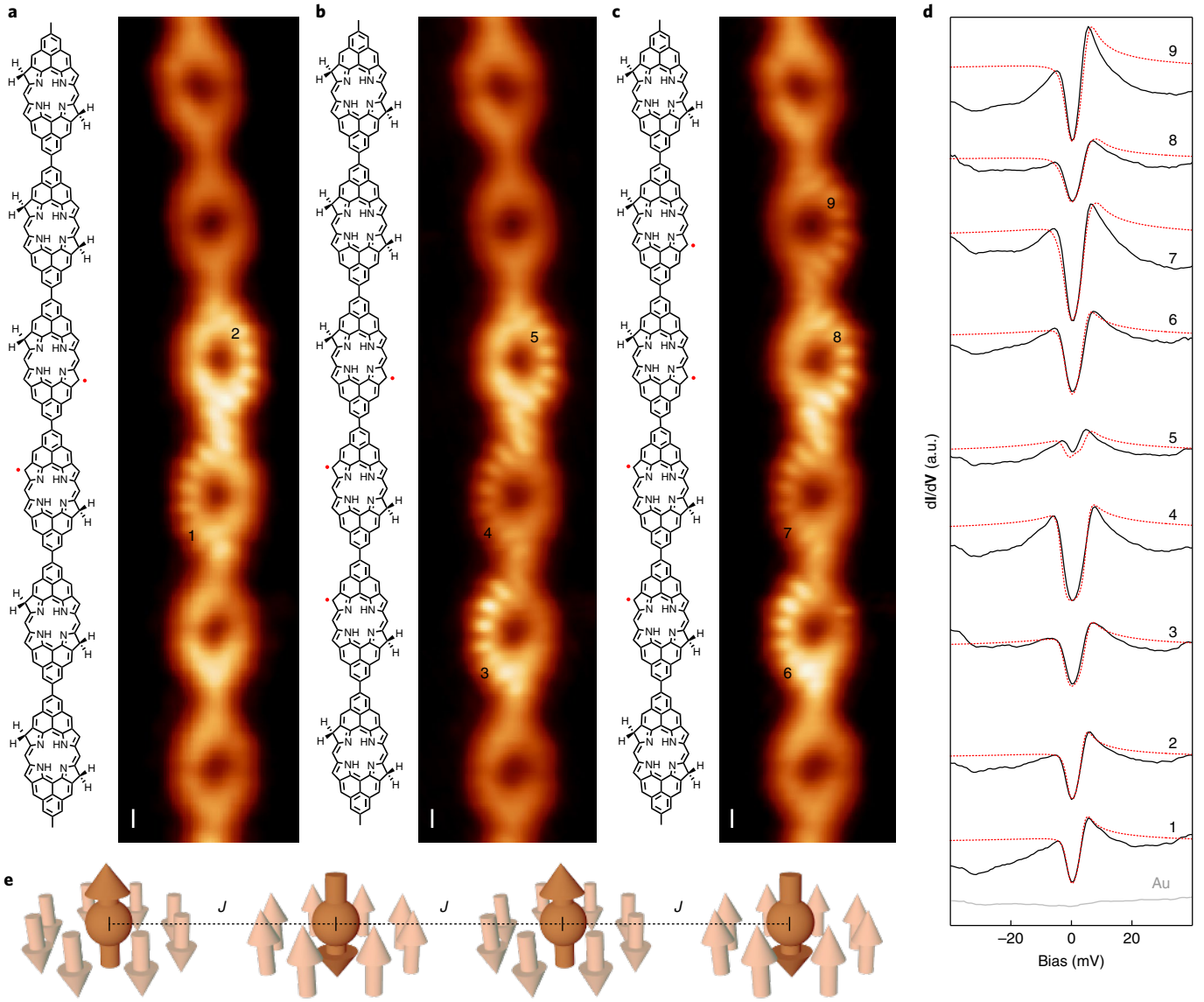

Fig. 4 | Antiferromagnetic coupled finite $S = 1/2$ spin chain. **a**–**c**, Characterization of $S = 1/2$ antiferromagnets: dimer (**a**), trimer (**b**) and tetramer (**c**). Left, chemical structure; right, constant-height current image (bias, 10 mV; scale bars, 0.25 nm). **d**, dI/dV spectra (black solid lines) taken at the locations marked in the constant-height current images in **a**–**c** and curves fitted by a perturbative approach using the code reported by in ref. [39] (red dashed lines). The dip features indicate that the short $S = 1/2$ spin chains host a finite excitation gap, in agreement with the Heisenberg model. **e**, Schematic of an $S = 1/2$ antiferromagnet on Au(111). The dark orange arrows represent the spins of the molecules, the light orange arrows represent the spin of the screening conduction electrons of Au(111), and J is the inter-unit magnetic coupling strength.

Fig. 14). In the following step, a third spin was introduced into the system. After positioning the tip over the right unit, two steps are observed at 3 mV and 20 mV due to the presence of inelastic tunnelling channels originating from the inter- and intra-unit spin-flip process (spectrum 4 in Fig. 3d). Similar observations were made for the tetra-radical dimer, confirming intra-unit ferromagnetic coupling and intra-unit antiferromagnetic coupling (spectra 6 and 7 in Fig. 3d). As illustrated in Fig. 3e, we modelled the magnetic exchange interactions among the four spins in the dimer by considering an intra-unit coupling of −20 meV and inter-unit couplings of 3.2 meV (same side) and 2.4 meV (opposite side). As shown in Fig. 2d, the simulated spectra obtained using the code reported in ref. [39] agree well with the STS measurements, confirming that the created spins are coupled together. Because the intra-unit coupling J_1 is significantly larger than inter-unit couplings J_2 and J_3, the low-lying spin states of the tetra-spin $S = 1/2$ system in a porphyrin dimer can also be described by a bilinear–biquadratic $S = 1$ model. To fit the low-lying spin states, an effective magnetic coupling of $J = 2.8$ meV and $\beta = 0.001$ J was obtained, suggesting that the tetra-spin $S = 1/2$ system can be simplified as an antiferromagnetic $S = 1$ system (illustrated in Fig. 3e).

Spin $S = 1/2$ antiferromagnetic quantum nanomagnets

The spin $S = 1/2$ antiferromagnets were constructed one by one in a long porphyrin polymer, as shown in Fig. 4. We probed the excitation gap of $S = 1/2$ antiferromagnets of different lengths by means of inelastic tunnelling spectroscopy. As shown in Fig. 4d, a dip-like feature can be observed in the site-resolved dI/dV spectra; this can be attributed to the presence of the first excitation gap of the spin systems, that is, the energy difference between the ground state and the first excited state as excited by inelastic tunnelling electrons. To better determine the excitation energy positions, we took the numerical derivation of all the dI/dV spectra and found that the spin-flip energy positions remain constant,

https://doi.org/10.1038/s41557-022-01061-5

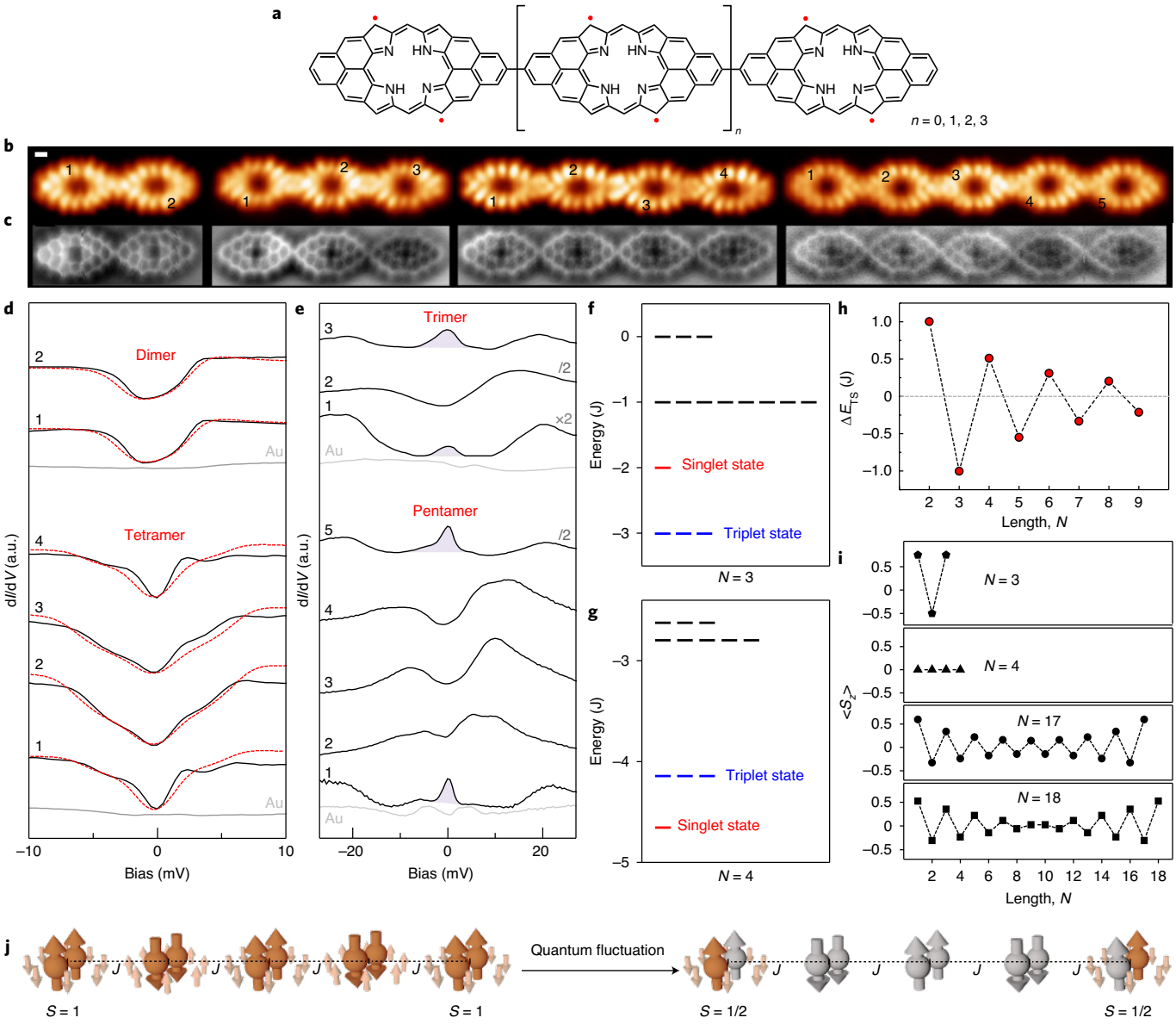

Fig. 5 | Antiferromagnetic coupled finite $S = 1$ spin chains. a–**c**, Chemical structure (**a**), constant-height current image (**b**) (bias voltage, 10 mV; scale bar, 0.25 nm) and nc-AFM images (**c**) (resonant frequency, 28 kHz; oscillation amplitude, 100 pm) of $S = 1$ antiferromagnets of different lengths. **d**, d*I*/d*V* spectra taken on the even-numbered chains marked in **b** (solid lines) and fitted spectra using a perturbative approach (dashed lines). **e**, d*I*/d*V* spectra taken on the odd-numbered chains marked in **b**. Even-numbered chains show a finite gap, while odd-numbered chains show an end Kondo resonance. **f**,**g**, Low-lying spin states of the $N = 3$ (**f**) and $N = 4$ (**g**) spin $S = 1$ chain, as calculated by the Heisenberg model. The different spectroscopic features between even- and odd-numbered chains originate from their different ground states. **h**, Calculated energy difference between the triplet state and singlet state as a function of chain length N. The triplet and singlet states become degenerate for infinitely long chains. **i**, Calculated average magnetization in z direction $\langle S_z \rangle$ for the $N = 3$, 4, 17 and 18 $S = 1$ spin chains. For $N = 3$, 4 and 17, the average magnetization is calculated using its ground state. For the $N = 18$ chain, the average magnetization is calculated using its first excited triplet states, considering the ground singlet state and the first excited triplet states are nearly degenerate. **j**, Schematic model showing the presence of edge spins in an $N = 5$ spin chain: quantum fluctuations convert the antiferromagnetic $S = 1$ spin chain (left) into a topological $S = 1$ phase with spin cancelled in the bulk and the emergence of $S = 1/2$ end states.

although the peak intensity varies significantly when positioning the tip over different positions within a unit (see the site-dependent d*I*/d*V* spectra in Supplementary Fig. 6). Apparently, our constructed spin $S = 1/2$ antiferromagnets cannot be explained by the classic Ising model, where the energy required to flip a spin in the centre is two times larger than that at the two termini of a spin chain. This deviation from the Ising model originates from the extremely weak spin-orbital coupling of the carbons, which results in a negligible magnetic anisotropy energy. In this case, the physics of our constructed molecular nanomagnets is dominated by quantum effects and can be captured by the Heisenberg antiferromagnet $S = 1/2$ model[44]. Considering the coupling with Au(111) itinerant electrons and the scattering process of the tunnelling electrons, these dip features can be satisfactorily reproduced by such modelling using the code reported in ref. [39] (detailed fitting parameters are presented in Supplementary Fig. 17). Interestingly, we notice that Coulomb scattering between the molecule and substrate is site-dependent, similar to the behaviour observed for porphyrins on Pb(111)[45].

Spin S = 1 antiferromagnetic quantum nanomagnets

Spin S = 1 antiferromagnets of different length were constructed and studied thoroughly (Fig. 5). The S = 1 antiferromagnetic spin chain is a prototype of fractional and topological phase, as proposed by Haldane in the 1980s (also known as the Haldane spin chain). According to the Haldane conjecture, such a spin chain is a topological insulator due to quantum fluctuations (the random change of system's energy due to the uncertainty principle), with all spins cancelled in the bulk and spin-1/2 edge states at the ends[46]. Finite-size S = 1 antiferromagnets of up to five units were constructed to obtain size-dependent magnetic excitations. Figure 5d,e shows site-resolved dI/dV spectra taken for the finite S = 1 chains; these show spectral features that are distinct for the even- and odd-numbered chains. With even-numbered chains, step-like features are observed at all units, with the first excitation gap decreasing from 2.4 meV to 1.1 meV as the length increases from two to four units. With odd-numbered chains, a zero-bias peak is observed at the terminal units, and a dip-like feature in the bulk units. The magnetic-field-dependent dI/dV measurements show that the zero-bias peak is robust against a magnetic field of up to 3 T, and the temperature dependent dI/dV measurements show that the peak width broadens with increasing temperature. In the single-impurity Anderson model, the Kondo peak width reflects the magnetic exchange strength between spin impurities and itinerant electrons as obtained by Fermi liquid theory, which agrees well with our observations, giving a Kondo temperature of 21 K (Supplementary Fig. 7). Because this behaviour clearly deviates from that of an underscreened high spin S = 1 in odd-numbered chains, we attribute the presence of the zero-bias peak at the terminal units to Kondo screening of the end S = 1/2 spins. The detection of end S = 1/2 spins in S = 1 spin chains indicates that quantum fluctuations transform the antiferromagnetic S = 1 spin chain into a topological phase with spin cancelled in the bulk and the emergence of end states, as proposed by Haldane (Fig. 5j).

A Heisenberg antiferromagnetic S = 1 model was used to elucidate our observations. In a Haldane chain, the considered length is long enough that the ground state is a four-fold degenerate edge state that contains one singlet level and three triplet levels. For short chains, S = 1 Heisenberg model calculations show that (1) the ground state of odd-numbered chains is the three-fold degenerate triplet edge state, and the first excited state is the singlet state; (2) the ground state of even-numbered chain is the singlet edge state, and the first excited state is the three-fold degenerate triplet edge state (Fig. 5f,g and Supplementary Fig. 16); (3) the energy difference between the triplet and singlet state decreases exponentially with increasing length and approaches to zero for infinitely long chains (Fig. 5h). We attribute the observed distinct zero-energy features of even- and odd-numbered spin chains to their different ground states, according to Heisenberg model calculations. As shown in Fig. 5i, we calculated the local average magnetization $\langle S_z \rangle$ on each unit by using the singlet and triplet ground states with $|S, S_z\rangle = |1, +1\rangle$ and $|S, S_z\rangle = |0, +1\rangle$, respectively. For even-numbered chains, the average magnetization $\langle S_z \rangle$ on all the units is always zero, which explains the absence of a zero-bias peak due to the singlet ground state. For odd-numbered chains, the average magnetization $\langle S_z \rangle$ on each unit is non-zero, with dominant weight on the two end units due to the triplet ground state, which causes the zero-bias Kondo resonances. Once the chains are long enough that the singlet and triplet states are nearly degenerate, the zero-bias peak can be observed in both odd- and even-numbered chains (Fig. 5i).

Conclusion

In summary, we have demonstrated an effective approach to building molecular quantum nanomagnets in metal-free porphyrins on Au(111), with the ultimate ability to arrange coupled spins, one by one, at predefined locations. The quantum magnetism behaviours of the constructed nanomagnets have been demonstrated by scanning probe techniques, together with theory calculations. Owing to the delocalized character of π radicals, significant intra- and inter-unit magnetic exchange interactions have been observed, with values up to −20 meV and 3 meV, respectively. Using our established strategy, we have constructed a series of S = 1/2 and S = 1 antiferromagnetic nanomagnets one by one, and traced their magnetic properties. A finite excitation gap was observed for S = 1/2 nanomagnets, consistent with the S = 1/2 Heisenberg antiferromagnetic model. Interestingly, we observed an end state for S = 1 nanomagnets with odd-numbered units, which is attributed to the presence of the triplet ground state. Our work provides a widely engineerable platform to further explore the exotic phases of quantum magnetism in real space, such as magnetic plateaux, spin liquid states or spin–Peierls states.

Online content

Any methods, additional references, Nature Research reporting summaries, source data, extended data, supplementary information, acknowledgements, peer review information; details of author contributions and competing interests; and statements of data and code availability are available at https://doi.org/10.1038/s41557-022-01061-5.

References

1. Auwärter, W., Écija, D., Klappenberger, F. & Barth, J. V. Porphyrins at interfaces. *Nat. Chem.* **7**, 105–120 (2015).
2. Shimizu, D. & Osuka, A. Porphyrinoids as a platform of stable radicals. *Chem. Sci.* **9**, 1408–1423 (2018).
3. Li, J. et al. Survival of spin state in magnetic porphyrins contacted by graphene nanoribbons. *Sci. Adv.* **4**, eaaq0582 (2018).
4. Kadish, K., Smith, K. & Guilard, R. *Handbook of Porphyrin Science* (World Scientific, 2010).
5. Baklanov, A. et al. On-surface synthesis of nonmetal porphyrins. *J. Am. Chem. Soc.* **142**, 1871–1881 (2020).
6. Mateo, L. M. et al. On-surface synthesis and characterization of triply fused porphyrin-graphene nanoribbon hybrids. *Angew. Chem. Int. Ed.* **59**, 1334–1339 (2020).
7. Fan, Q. et al. Template-controlled on-surface synthesis of a lanthanide supernaphthalocyanine and its open-chain polycyanine counterpart. *Nat. Commun.* **10**, 5049 (2019).
8. Doppagne, B. et al. Single-molecule tautomerization tracking through space- and time-resolved fluorescence spectroscopy. *Nat. Nanotechnol.* **15**, 207–211 (2020).
9. Köbke, A. et al. Reversible coordination-induced spin-state switching in complexes on metal surfaces. *Nat. Nanotechnol.* **15**, 18–21 (2020).
10. Cirera, B. et al. On-surface synthesis of gold porphyrin derivatives via a cascade of chemical interactions: planarization, self-metalation and intermolecular coupling. *Chem. Mater.* **31**, 3248–3256 (2019).
11. Su, X., Xue, Z., Li, G. & Yu, P. Edge state engineering of graphene nanoribbons. *Nano Lett.* **18**, 5744–5751 (2018).
12. Bischoff, F. et al. Exploration of interfacial porphine coupling schemes and hybrid systems by bond-resolved scanning probe microscopy. *Angew. Chem. Int. Ed.* **57**, 16030–16035 (2018).
13. Zeng, W. et al. Phenalenyl-fused porphyrins with different ground states. *Chem. Sci.* **6**, 2427–2433 (2015).
14. Sun, Q. et al. On-surface formation of two-dimensional polymer via direct C–H activation of metal phthalocyanine. *Chem. Commun.* **51**, 2836–2839 (2015).
15. Müllegger, S., Schöfberger, W., Rashidi, M., Reith, L. M. & Koch, R. Spectroscopic STM studies of single gold(III) porphyrin molecules. *J. Am. Chem. Soc.* **131**, 17740–17741 (2009).
16. Grill, L. & Hecht, S. Covalent on-surface polymerization. *Nat. Chem.* **12**, 115–130 (2020).
17. Grill, L. et al. Nano-architectures by covalent assembly of molecular building blocks. *Nat. Nanotechnol.* **2**, 687–691 (2007).

18. Zhao, Y. et al. Precise control of π-electron magnetism in metal-free porphyrins. *J. Am. Chem. Soc.* **142**, 18532–18540 (2020).
19. Rana, A. et al. Stable expanded porphycene-based diradicaloid and tetraradicaloid. *Angew. Chem.* **130**, 12714–12717 (2018).
20. Sun, Q. et al. Inducing open-shell character in porphyrins through surface-assisted phenalenyl π-extension. *J. Am. Chem. Soc.* **142**, 18109–18117 (2020).
21. Clair, S. & de Oteyza, D. G. Controlling a chemical coupling reaction on a surface: tools and strategies for on-surface synthesis. *Chem. Rev.* **119**, 4717–4776 (2019).
22. Ruffieux, P. et al. On-surface synthesis of graphene nanoribbons with zigzag edge topology. *Nature* **531**, 489–492 (2016).
23. Cai, J. et al. Atomically precise bottom-up fabrication of graphene nanoribbons. *Nature* **466**, 470–473 (2010).
24. Gröning, O. et al. Engineering of robust topological quantum phases in graphene nanoribbons. *Nature* **560**, 209–213 (2018).
25. Zhong, D. et al. Linear alkane polymerization on a gold. *Surf. Sci.* **334**, 213–216 (2011).
26. de Oteyza, D. G. et al. Direct imaging of covalent bond structure in single-molecule chemical reactions. *Science* **340**, 1434–1437 (2013).
27. Moreno, C. et al. Bottom-up synthesis of multifunctional nanoporous graphene. *Science* **360**, 199–203 (2018).
28. Mishra, S. et al. Topological frustration induces unconventional magnetism in a nanographene. *Nat. Nanotechnol.* **15**, 22–28 (2020).
29. Zheng, Y. et al. Designer spin order in diradical nanographenes. *Nat. Commun.* **11**, 6076 (2020).
30. Zheng, Y. et al. Engineering of magnetic coupling in nanographene. *Phys. Rev. Lett.* **124**, 147206 (2020).
31. Song, S. et al. On-surface synthesis of graphene nanostructures with π-magnetism. *Chem. Soc. Rev.* **50**, 3238–3262 (2021).
32. Hla, S.-W., Bartels, L., Meyer, G. & Rieder, K.-H. Inducing all steps of a chemical reaction with the scanning tunneling microscope tip: towards single molecule engineering. *Phys. Rev. Lett.* **85**, 2777–2780 (2000).
33. Kaiser, K. et al. An *sp*-hybridized molecular carbon allotrope, cyclo[18]carbon. *Science* **365**, 1299–1301 (2019).
34. Pavliček, N. et al. Synthesis and characterization of triangulene. *Nat. Nanotechnol.* **12**, 308–311 (2017).
35. Pavliček, N. et al. Polyyne formation via skeletal rearrangement induced by atomic manipulation. *Nat. Chem.* **10**, 853–858 (2018).
36. Beyer, D. et al. Graphene nanoribbons derived from zigzag edge-encased poly(para-2,9-dibenzo[bc,kl]coronenylene) polymer chains. *J. Am. Chem. Soc.* **141**, 2843–2846 (2019).
37. Gross, L., Mohn, F., Moll, N., Liljeroth, P. & Meyer, G. The chemical structure of a molecule resolved by atomic force microscopy. *Science* **325**, 1110–1114 (2009).
38. Ortiz, R. et al. Exchange rules for diradical π-conjugated hydrocarbons. *Nano Lett.* **19**, 5991–5997 (2019).
39. Ternes, M. Spin excitations and correlations in scanning tunneling spectroscopy. *New J. Phys.* **17**, 063016 (2015).
40. Choi, D.-J. et al. Colloquium: atomic spin chains on surfaces. *Rev. Mod. Phys.* **91**, 041001 (2019).
41. Li, J. et al. Uncovering the triplet ground state of triangular graphene nanoflakes engineered with atomic precision on a metal surface. *Phys. Rev. Lett.* **124**, 177201 (2020).
42. Su, X. et al. Atomically precise synthesis and characterization of heptauthrene with triplet ground state. *Nano Lett.* **20**, 6859–6864 (2020).
43. Žonda, M. et al. Resolving ambiguity of the Kondo temperature determination in mechanically tunable single-molecule Kondo systems. *J. Phys. Chem. Lett.* **12**, 6320–6325 (2021).
44. Toskovic, R. et al. Atomic spin-chain realization of a model for quantum criticality. *Nat. Phys.* **12**, 656–660 (2016).
45. Rubio-Verdú, C., Zaldívar, J., Žitko, R. & Pascual, J. I. Coupled Yu-Shiba-Rusinov states induced by a many-body molecular spin on a superconductor. *Phys. Rev. Lett.* **126**, 017001 (2021).
46. Haldane, F. D. M. Nonlinear field theory of large-spin Heisenberg antiferromagnets: semiclassically quantized solitons of the one-dimensional easy-axis Néel state. *Phys. Rev. Lett.* **50**, 1153–1156 (1983).

Publisher's note Springer Nature remains neutral with regard to jurisdictional claims in published maps and institutional affiliations.

Springer Nature or its licensor holds exclusive rights to this article under a publishing agreement with the author(s) or other rightsholder(s); author self-archiving of the accepted manuscript version of this article is solely governed by the terms of such publishing agreement and applicable law.

© The Author(s), under exclusive licence to Springer Nature Limited 2022

Methods

On-surface synthesis and characterization

Under ultrahigh-vacuum (3×10^{-10} mbar) conditions, a commercially available low-temperature Joule–Thomson scanning probe microscope was used for sample preparation and characterization. The Au(111) single crystal was cleaned cyclically by argon ion sputtering, then annealed to 800 K to obtain atomically flat terraces. The molecular precursors of 5,15-bis(4-bromo-2,6-dimethylphenyl)porphyrin and 5-(2,6-dimethylphenyl)porphyrin were thermally deposited on the clean Au(111) surface at 180 °C, then annealed to 290 °C for 10 min. The sample was subsequently transferred to a cryogenic scanner at 1.36 K for characterization. Carbon monoxide molecules were dosed onto the cold sample at ~12 K (1.5×10^{-8} mbar, 1 min). To improve the resolution of STM/AFM imaging, the CO molecule was picked up from the Au surface onto the apex of the tungsten tip. In nc-AFM imaging, a quartz tuning fork with a resonance frequency of 28 kHz was used. A lock-in amplifier (521 Hz, 1 mV modulation) was used to obtain d*I*/d*V* spectra. The spectra were taken at 1.36 K unless otherwise stated. The STM and nc-AFM images were processed with WSxM software.

Synthetic procedure for 5,15-bis(4-bromo-2,6-dimethylphenyl)porphyrin in solution

A solution of dipyrromethane (1.75 g, 12 mmol) and 2,6-dimethyl-4-bromobenzaldehyde (12 mmol) in $CHCl_3$ (1.2 l) was treated with $BF_3{\cdot}OEt_2$ (1 ml) at room temperature. The flask was shielded from light with aluminium foil, and the solution was stirred under argon for 8 h. Subsequently, 2,3-dicyano-5,6-dichlorobenzoquinone (4.09 g, 18 mmol) was added and the mixture was stirred at room temperature for 0.5 h. The mixture was neutralized with triethylamine (15 ml). The volume of the solvent was reduced to ~300 ml under reduced pressure, then the mixture was filtered through a pad of basic alumina (Merck, aluminium oxide 90 active basic). The filtrate was concentrated and the residue chromatographed on silica gel. The eluate was then evaporated and the resulting solid purified by recrystallization from CH_2Cl_2/hexane to afford the product (25%)[47].

DFT calculations in the gas phase

Spin-polarized DFT calculations were performed using the Gaussian 16 package. The PBE0-D3 (BJ) functional was applied to show the electronic structure of all gas-phase molecular nanomagnets[48], and using the def2-SVP basis set for geometry optimization, which was extended to a def2-TZVP basis set for the single-point energy calculation[49]. The electronic structures of molecules were calculated using the restricted and unrestricted methods for different spin multiplicities. Molecular orbitals and electron spin density distributions were analysed by Multiwfn[50]. Images of the structures and isosurfaces were plotted using VESTA[51].

DFT calculations with the Au substrate

Periodic DFT calculations are performed with the VASP package[52–54], relying on the spin-polarized, van der Waals inclusive functional devised by Dion and others[55]. Electron–core interactions are accounted for through the projector augmented wave method[56]. We used a cutoff kinetic energy of 400 eV and a single *k* point. The models consist of porphyrin dimers supported on a hexagonal supercell of Au(111) of size 45.99 Å × 20.12 Å and contain 526 atoms, with the Au(111) substrate described by four slabs of Au atoms. All atomic coordinates are optimized with a tolerance on forces of 25 meV $Å^{-1}$, except the three slabs of Au farthest from the porphyrins, which are constrained to their equilibrium position in the bulk Au(111).

Theoretical modelling

To understand the scattering and screening effects in the STM junction, we fitted our d*I*/d*V* spectra using the perturbation approach up to third order, as developed by Ternes[57]. We calculated the spin states of finite $S = 1$ spin chains using a bilinear–biquadratic model. The Hamiltonian is

$$\hat{H} = \mathrm{J}\sum_{\langle ij\rangle}\vec{S}_i\vec{S}_j + \beta\left(\vec{S}_i\vec{S}_j\right)^2,$$

where J is the magnetic coupling strength between two spins $\vec{S}_i$ and $\vec{S}_j$, and β is the strength of the biquadratic term relative to the bilinear term.

Data availability

Data supporting the findings of this study are available within the paper and its Supplementary Information. The Supplementary Information includes details of experiments, synthetic procedures and characterization data of the molecular precursor, as well as details of calculations. Source data are provided with this paper.

Code availability

The Heisenberg Hamiltonians were solved using Python. Details of this code are available from the corresponding author on request.

References

47. Taniguchi, M., Balakumar, A., Fan, D., McDowell, B. E. & Lindsey, J. S. Imine-substituted dipyrromethanes in the synthesis of porphyrins bearing one or two meso substituents. *J. Porphyr. Phthalocyan.* **09**, 554–574 (2005).
48. Grimme, S., Antony, J., Ehrlich, S. & Krieg, H. A consistent and accurate ab initio parametrization of density functional dispersion correction (DFT-D) for the 94 elements H-Pu. *J. Chem. Phys.* **132**, 154104 (2010).
49. Weigend, F. & Ahlrichs, R. Balanced basis sets of split valence, triple zeta valence and quadruple zeta valence quality for H to Rn: design and assessment of accuracy. *Phys. Chem. Chem. Phys.* **7**, 3297–3305 (2005).
50. Lu, T. & Chen, F. Multiwfn: a multifunctional wavefunction analyzer. *J. Comput. Chem.* **33**, 580–592 (2012).
51. Momma, K. & Izumi, F. VESTA 3 for three-dimensional visualization of crystal, volumetric and morphology data. *J. Appl. Crystallogr.* **44**, 1272–1276 (2011).
52. Kresse, G. & Hafner, J. Ab initio molecular dynamics for liquid metals. *Phys. Rev. B* **47**, 558–561 (1993).
53. Kresse, G. & Furthmüller, J. Efficient iterative schemes for ab initio total-energy calculations using a plane-wave basis set. *Phys. Rev. B* **54**, 11169–11186 (1996).
54. Kresse, G. & Furthmüller, J. Efficiency of ab-initio total energy calculations for metals and semiconductors using a plane-wave basis set. *Comput. Mater. Sci.* **6**, 15–50 (1996).
55. Dion, M., Rydberg, H., Schröder, E., Langreth, D. C. & Lundqvist, B. I. Van der Waals density functional for general geometries. *Phys. Rev. Lett.* **92**, 246401 (2004).
56. Blöchl, P. E. Projector augmented-wave method. *Phys. Rev. B* **50**, 17953–17979 (1994).
57. Ternes, M., Heinrich, A. J. & Schneider, W.-D. Spectroscopic manifestations of the Kondo effect on single adatoms. *J. Phys. Condens. Matter* **21**, 053001 (2009).

Acknowledgements

S.W. acknowledges financial support from the National Key R&D Program of China (no. 2020YFA0309000), the National Natural Science Foundation of China (nos. 11874258 and 12074247), the Shanghai Municipal Science and Technology Qi Ming Xing Project (no. 20QA1405100), Fok Ying Tung Foundation for young researchers and SJTU (no. 21×010200846). This work is also partially supported by the Ministry of Science and Technology of China (grants nos. 2019YFA0308600, 2016YFA0301003 and 2016YFA0300403), NSFC

(grants nos. 11521404, 11634009, 92065201, 11874256, 11790313 and 11861161003), the Strategic Priority Research Program of Chinese Academy of Sciences (grant no. XDB28000000) and the Science and Technology Commission of Shanghai Municipality (grants nos. 2019SHZDZX01, 19JC1412701 and 20QA1405100). We acknowledge the π 2.0 cluster of the Center for High Performance Computing at Shanghai Jiao Tong University.

Author contributions

S.W. conceived the experiments. Y.Z., C. Li and G.Z. performed the SPM experiments. K.J. and X.Z. synthesized the molecular precursors. Y. Liu performed the DFT calculations in the gas phase. M.P. and E.K. performed the DFT calculations on Au(111). C. Li and M.Q. performed the modelling calculations. D.G., Y. Li, H.Z., C. Liu and J.J. analysed the STS data. S.W., Y.Z. and C. Li wrote the paper. All authors discussed the results and implications and commented on the manuscript at all stages.

Competing interests

The authors declare no competing interests.

Additional information

Supplementary information The online version contains supplementary material available at https://doi.org/10.1038/s41557-022-01061-5.

Correspondence and requests for materials should be addressed to Xiaodong Zhuang or Shiyong Wang.

Peer review information *Nature Chemistry* thanks Pavel Jelinek, Jiong Lu, Oleg Yazyev and the other, anonymous, reviewer(s) for their contribution to the peer review of this work.

Reprints and permissions information is available at www.nature.com/reprints.